ORIGINAL PAPER

Preparation and Characterization of nZVI, Bimetallic Fe^0-Cu, and Fava Bean Activated Carbon-Supported Bimetallic AC-Fe^0-Cu for Anionic Methyl Orange Dye Removal

A. B. Abdel-Aziz[1] · Nora Mohamed[5] · Reem M. El-taweel[2] · Husien Sh[2] · Alyaa I. Salim[3] · Kaushik Pal[4] ·
Irene Samy Fahim[5] · Lobna A. Said[6] · Ahmed G. Radwan[2,7]

Abstract

Nano zero-valent iron (nZVI), bimetallic Nano zero-valent iron-copper (Fe^0- Cu), and fava bean activated carbon-supported with bimetallic Nano zero-valent iron-copper (AC-Fe^0-Cu) were prepared and characterized by DLS, FT-IR, XRD, and SEM. The influence of the synthesized adsorbents on the adsorption and removal of soluble anionic methyl orange (M.O) dye was investigated using UV-V spectroscopy. The influence of numerous operational parameters was studied at varied pH (3–9), time intervals (15–180 min), and dye concentrations (25–1000 ppm) to establish the best removal conditions. The maximum removal efficiency of M.O. using the prepared adsorbent materials reached about 99%. The removal efficiency is modeled using response surface methodology (RSM). The Bimetallic Fe^0-Cu, the best experimental and predicted removal efficiency is 96.8% RE. For the H2SO4 chemical AC-Fe^0-Cu, the best experimental and removal efficiency is 96.25% RE. The commercial AC-Fe0–Cu, the best experimental and predicted removal efficiency is 94.93%RE. This study aims to produce low-cost adsorbents such as Bimetallic Fe0-Cu, and Fava Bean Activated Carbon-Supported Bimetallic AC-Fe0-Cu to treat the industrial wastewater from the anionic methyl orange (M.O) dye and illustrate its ability to compete H2SO4 chemical AC-Fe0-Cu, and commercial AC-Fe0-Cu.

Keywords Adsorption · Response surface methodology (RSM) · Artificial neural network (ANN) · Moth search algorithm (MSA)

✉ Kaushik Pal
kaushikphysics@gmail.com

✉ Irene Samy Fahim
ISamy@nu.edu.eg

1   October High Institute for Engineering and Technology, Giza, Egypt

2   School of Engineering and Applied Sciences, Nile University, Giza, Egypt

3   Basic Science Department, School of Engineering and Applied Science, Nile University, Giza, Egypt

4   Department of Physics, University Centre for Research and Development, Chandigarh University, Mohali, Gharuan, Punjab, India

5   Industrial Engineering Program, SESC Research Center, NileUniversity, Giza, Egypt

6   Nanoelectronics Integrated Systems Center (NISC), Nile University, Giza, Egypt

7   Engineering Mathematics and Physics Dept., Faculty of Engineering, Cairo University, Giza 12613, Egypt

Abbreviations

nZVI	Nano zero-valent iron
mZVI	Modified microscale zero-valent iron
M.O	Methyl orange
AC	Activated carbon
RSM	Response surface methodology
ANN	Artificial neural network
MSA	Moth search algorithm
DEO	Differential evolution optimization
DLS	Dynamic light scattering
FTIR	Fourier transition infrared
XRD	X-ray diffraction
SEM	Scanning electron microscope
SNNs	Simulated neural networks
DR	Dubinin-Radushkeivch
PFO	The mean free energy
PSO	Pseudo-Second-Order
E	Mean free energy

1 Introduction

Various methods like adsorption, chemical precipitation, membrane filtration and electrodialysis were used to treat wastewater. Adsorption is one of the most efficient techniques for treating wastewater because of its advantages of high removal efficiency and ease of operation [1]. Heavy metals and colors are removed from wastewater using several adsorbents such as activated carbon, agricultural wastes, sawdust, zeolite, and clay [2]. However, these adsorbents frequently need additional separation stages with high, which limited their applicability. Nano zero-valent iron (nZVI) gained a lot of attention for environmental applications, because of its high reactivity, low cost, availability, ease of separation, and presence of many active sites [3]. NZVI has various physical features that enable it to remove heavy metals and colors from industrial effluent. It was discovered that nZVI outperformed both mZVI and iron oxide particles when evaluating how well they remove dyes. This was illustrated in depth using a critical physical feature, the available active surface area. Where nZVI has a surface area of roughly (29.67 m2/g) and mZVI has a substantially smaller sur- face area (2.55 m2/g). Using these particles, it was revealed that the efficiency of nZVI was 90%, but the efficiency of mZVI was just 25% [4]. Additionally, nZVI particles have a strong tendency to destroy textile colors [5, 6] and also have a number of chemical features that make them more efficient at degrading colors found during industrial wastewater. The nZVI particles have a vital reaction that degraded the dyes and formed of other simpler chemicals or related compounds. The connection between nZVI and dyes formed when the nZVI (electron donor) lost electrons, which were subsequently taken up by the dye molecules (electron acceptor) [7]. In aqueous environments, the nZVI particles transformed to ferrous Fe^{2+} and ferric Fe^{3+} ions, which subsequently reacted with hydroxyl ions in those solutions as a result of oxidation and reduction re- actions between them and also reacted with the dyes to break the chromophore ($-N=N-$) link [8]. The auxochrome connection was likewise broken by the nZVI particles, which removed the color of dye molecules [9].

Bimetallic nanoparticles were in a nanoscale, which consisted of mixtures of two different metals. When two metals were combined, they can retain the properties of their constituents while also gaining better attributes as a result of the joining process. Bimetallic nanoparticles' properties were influenced by their size, structure, and morphology [10]. The presence of a small fraction of transition metals with nZVI acted as a reducing agent, speeding up the surface reaction to remove organic molecules and other contaminants [11]. Researchers used different transition elements in recent years to see the most efficient for re-moving colors and heavy metal ions from industrial effluent. Bimetallic Nano zero-valent iron-copper (Fe^0-Cu) attracted much attention due to the high efficiency seen in their performance to remove colors [12].

The initial concentration of dyes was one of the most important aspects for selecting the adsorption technique used to treat industrial wastewater. The adsorption efficiency decreased with increasing the dye content [13]. Pores, charges, hydrophilic or hydrophobic character, size, and distribution all affected adsorption effectiveness. It also depended on the surface area and whether functional groups were present or not [14, 15]. The magnetic property inherent in particular adsorbents provided outstanding and remarkable efficiency. This found in various treatments, such as using Nano ilmenite $FeTiO_3$ to remove cationic dyes like methylene blue with high effectiveness of up to 71.9 mg/g [16]. The contact time of the adsorbent materials with the industrial wastewater was critical in removing as many contaminants as feasible. By extending the contact time, the adsorption capacity of the adsorbent increased [17, 18].

Fava bean was widely consumed in several regions, including the Mediterranean region of Europe and Africa, as well as Latin America, China, and India. Fava bean peels were thrown out in large amounts. Just the small portion of such waste was used as animal feed by farmers [19]. Fava bean is one of Egypt's most important winter crops, being planted from the north to the south [20]. According to Egypt's Ministry of Agriculture and Land Reclamation, 194.259 tons of fava bean seeds were produced across 41.975 hectares in 2012/2013 [21]. For instance, the number of Egyptian beans imports was expected to in- crease from nearly 410 thousand tons in 2018 to about 500 thousand tons in 2025. The domestic production would decrease from about 144 thousand tons to about 16 thousand tons. Hence, beans consumption was expected to decrease from approximately 281 thousand tons in 2018 to about 72.5 thousand tons in 2025 [22]. Different activation techniques were used to produce activated carbon with different properties. In prior research, fava bean activated carbon powder was employed to remove heavy metal ions with high removal efficiencies [23]. Neural networks are considered one of the most important deep learning techniques, which are a subset of machine learning and are also known as artificial neural networks (ANNs) or simulated neural networks (SNNs) [24]. Their structure and nomenclature are modeled after the human brain, mirroring organic neuron communication. Each node, or artificial neuron, is linked to others and has its own weight and threshold. Any node whose output exceeds the defined threshold value is activated and begins sending data to the network's top layer. Otherwise, no data is transferred to the next network layer.

The artificial neural network (ANN) node layer is divided into three main types of layers, an input layer, an output layer, and one or more hidden layers. The concentration, dose, and time are considered the three main neurons of the input layer. The removal efficiency is considered a desired value and the only neuron inside the output layer. The hidden layer contains (3 to 15) neurons, the tenth neuron detected the least error of the most adsorption processes.

The input data are analyzed to be in the 0 to 1 range. The network's input variables were dosage, contact time, and temperature, while the network's output layer was removal efficiency. The experimental data set obtained by using the RSM was appropriate for evaluating the ANN model. The data set was split into three categories: 70% of the data is used to train the network, 15% for validation, and the balancing for testing the results. The network's performance was evaluated independently by the test set. The validation set altered the network's bias, variance, and generalization.

Response Surface Methodology (RSM) and Artificial Neural Network (ANN) combined with optimization algorithm are considered more effective for the opti- mization process [24]. The ANN model can learn linear, nonlinear and complex relationships between process variables [25]. ANN model is implemented to predict removal efficiency. The Moth search algorithm (MSA) is a metaheuristic algorithm applied to the ANN model to get optimum conditions that achieve maximum removal efficiency. Methyl Orange (M.O) removal by polyaniline- based nano-adsorbent was investigated in [26]. RSM was implemented to predict removal efficiency. Furthermore, ANN was integrated with differential evolution optimization (DEO) for the predic- tion of removal efficiency. ANN-DEO had better accuracy in prediction than RSM. However, the maximum removal efficiency was not evaluated. Furthermore, the polyaniline nano-adsorbent was used to adsorb M.O in [27]. ANN was implemented to predict the removal efficiency. OFAT was implemented to get the maximum removal efficiency. The M.O removal by lignin-derived zeolite templated carbon materials was optimized by RSM with Box–Behnken design [28]. RSM was used to find the most influential factor on the removal efficiency.

This study aims to produce low-cost adsorbents such as nZVI, Bimetallic Fe^0-Cu, and Fava Bean Activated Car- bon-Supported Bimetallic AC-Fe^0-Cu to treat the industrial wastewater from the anionic methyl orange (M.O) dye. RSM and ANN models predict the removal efficiency for differ- ent values for the factors. The maximum removal efficiency is evaluated by optimizing these mod- els. ANN is optimized by Moth Search Algorithm (MSA). These optimization tech- niques predict the maximum removal efficiency and the corre- sponding factor values. The optimization results are validated experimentally. Isotherm and kinetic models are implemented to understand the chemical characteristics. They provide information about the type of adsorption and the adsorbent surface. Furthermore, the maximum amount adsorbed can be estimated by them.

2 Experimental Work

2.1 Chemicals and Reagents

All used chemicals and reagents in the present work are high-grades, including ferric chloride hexahydrate ($FeCl_3.6H_2O$ 97% pure, LOBA Chemie), sodium borohydride ($NaBH_4$ 95% pure, ADVENT), copper chloride dihydrate ($CuCl_2.2H_2O$, BIOCHEM), charcoal activated (LOBA Chemie), ethanol (C_2H_5OH 96% pure), and methyl orange. Deionized H_2O is used for all experiments Fig. 1.

2.2 Preparation of Nano Zero Valent Iron (nZVI)

As shown in Eq. 1, the preparation procedure is based on the chemical reduction of ferric chloride hexahydrate $FeCl_3.6H_2O$ by sodium borohydride $NaBH_4$. Equivalent volumes of 0.1 M $FeCl_3.6H_2O$ solution and 0.5 M $NaBH_4$ solution are prepared in the laboratory for this approach. The ferric chloride solution in the conical flask is stirred constantly at 250 rpm. In contrast, a sodium borohydride solution is added drop by drop from the burette. After mixing, the solution is stirred for another 20 min. To ensure that the reduction reaction for the iron ions in the solution is finished. Following that, filtration is used to separate the produced precipitate, as shown in Fig. 2. The isolated precipitate is rinsed with deionized water three times and then with ethanol once. Finally, the product is dried at 70 and stored at room temperature under an ethanol layer [29].

$$2(FeCl_3.6H_2O) + 6NaBH_4 + 6H_2O \rightarrow 2Fe^0 + 21H2 + 6B(OH)_3 + 6NaCl \tag{1}$$
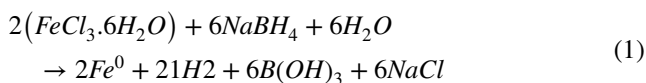
2.3 Preparation of Bimetallic (Fe⁰–Cu)

Using the co-precipitation method, a 0.002 M copper chloride dihydrate $CuCl_2.2H_2O$ solution is added to the $FeCl_3.6H_2O$ solution before adding the $NaBH_4$ solution from the burette under the same conditions [30]. The redox reaction between Cu^{2+} and nZVI is mostly determined by the reaction Eq. 2.

$$Fe^0 + Cu^{2+} \rightarrow Fe^{2+} + Cu^0 \tag{2}$$

2.4 Preparation of Fava Bean Activated Carbon (AC)

Fava bean peel waste is collected from local markets in Egypt. It is then washed, dried overnight at 105 °C, and ground into tiny pieces. Physical and chemical activation

Fig. 1 The graphical abstract illustrates the main steps of the brand-new manufacture technology of the low-cost adsorbents (nZVI)
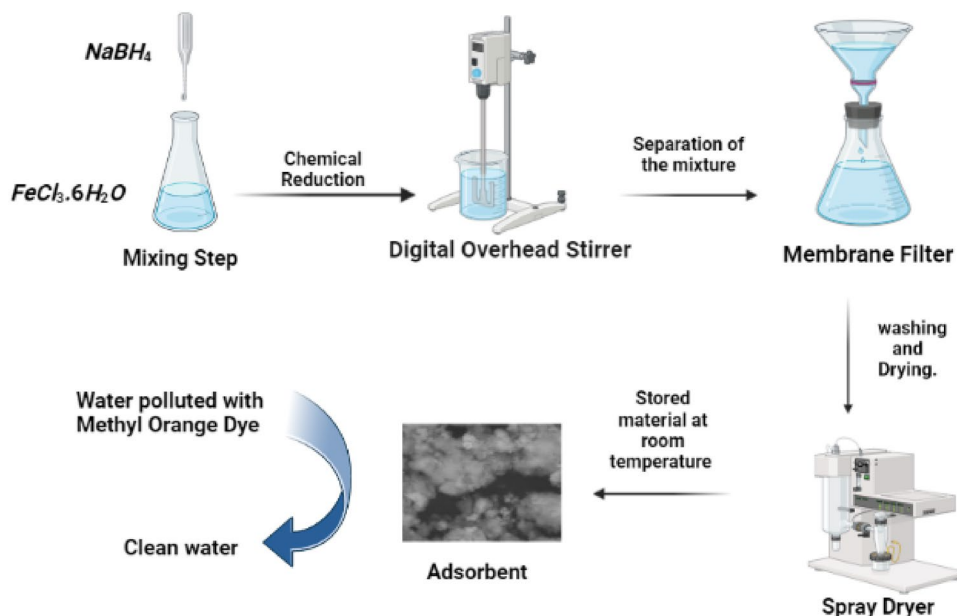
Fig. 2 Preparation steps of nZVI **a** Materials, **b** Titration & Stirring, **c** Filtration

(a)   (b)   (c)
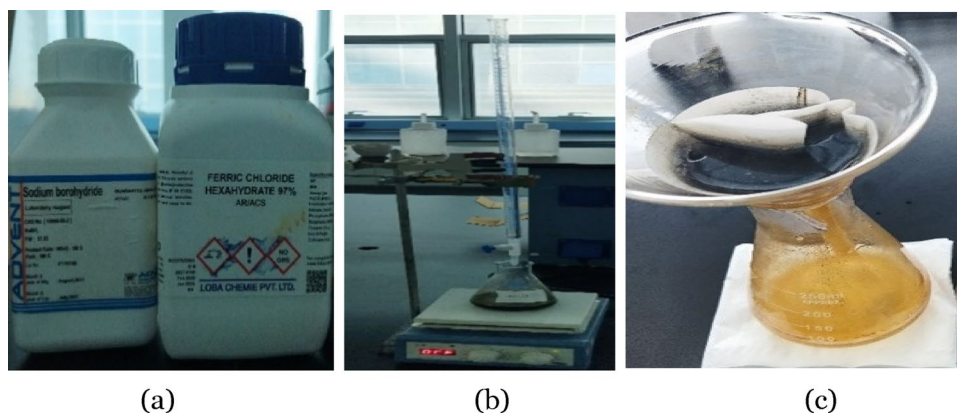
techniques are both accessible. Physical activation consists of a two-step process that begins with high-temperature carbonization and ends with activation. Chemical activation is a combined carbonization and activation process that takes one step at a low temperature.

2.4.1 Physical Activation

The fava bean peel waste is heat-treated at a high tem- perature after grinding thoroughly in the physical activation technique. 50 g of fava bean is placed in a muffle at 400 °C for one h, then at 600 °C for two h. Finally, for 15 min., the temperature is lowered to 300 °C. It is kept in a sealed bottle until it is used to protect the activated carbon (AC) from humid- ity [31, 32].

2.4.2 Chemical Activation

Different chemical activators are used in the chemical activation process. H_3PO_4 or H_2SO_4 are used as activators in two forms of activated carbon. 250 ml of 85% H_3PO_4 is added to 50 g fava bean peel waste, which is then mixed for 4 h at 85 °C on a magnetic stirrer before drying for 24 h at 110 °C [33]. The sample was then placed in a muffle for one hour at 600 °C, washed many times to obtain pH 7, and dried in an oven at 110 °C [34].

In the case of H_2SO_4 activation, 150 ml of 4 M H_2SO_4 is added to 50 g of fava bean peel waste and mixed at room temperature to make a homogeneous mix- ture [35]. After that, the mixture is placed for two h at 110 °C, then carbonized for three h at 400 °C, washed with deionized water until pH 7 is obtained, and dried in an oven at 110 °C [36].

2.5 Preparation of Fava Bean Activated Carbon-Supported Bimetallic (AC-F e⁰- Cu)

Before adding sodium borohydride, activated carbon-supported bimetallic (AC-F e0-Cu) is made by adding activated carbon to a ferric chloride solution (1 g/L of AC per a solution of 0.1 M FeCl3.6H2O and 0.002 M CuCl2.2H2O) [37]. Physically activated carbon, H2SO4 chemically activated carbon, H3PO4 chemically activated carbon, and commercial charcoal are used to make the (AC-F e0-Cu); moreover, the bimetallic particles are supported on the raw fava bean after grinding.

2.6 Adsorption Experiments

The efficiency of the produced compounds is tested using 1000 ppm methyl orange (MO) dye. The (MO) concentration is measured using a UV-V spec- trophotometer set at 465 nm. The removal efficiency is investigated using a pH range of 3 to 9, a contact time between the adsorbent material and MO ranging from 15 to 180 min., and methyl orange concentrations ranging from 25 to 1000 ppm. Shaking at 120 rpm and room temperature is used to carry out all adsorption processes [38]. The percentages of removal are computed using the equation below (Eq. 3):

$$Sorption[\%] = \left[C_0 - C_e\right]/C_0 \times 100 \tag{3}$$

where C_0 represents the initial concentration of M.O solution (mg/L) and C_e represents the equilibrium concentration of it (mg/L). The following Eq. 4 is used to compute the quantity of M.O dye extracted by the adsorbent material:

$$qe[mg/g] = [[C0 - Ce] \times V]/m \tag{4}$$

where q_e represents the equilibrium adsorption capacity (mg/g), V repre- sents the dye solution volume (L), and m represents the adsorbent mass (g).

2.7 Characterization of nZVI, Fe⁰-Cu and AC-Fe⁰-Cu

The size and charge of adsorbent material particles are determined using dynamic light scattering (DLS). The functional groups are identified using Fourier transition infrared (FT-IR). The structural groups of the adsorbent materials are demonstrated using X-ray diffraction (XRD) analysis. A scanning electron microscope (SEM) shows the surface morphology.

2.8 Adsorption Isotherms and Adsorption Kinetics Optimization

Models are built using response surface methodology (RSM) by setting up a series of experiment runs and fitting empirical models to data received under the specified design. Equation 5 is used to derive the anticipated responses.

$$Y = \beta_0 + \sum_{i=1}^{k} \beta_i x_i + \in \tag{5}$$

where Y represents the expected response, x_i represents the input variable, k represents the number of variables, β_0 represents the constant term, β_i repre- sents the linear coefficient, and ϵ represents the experimental residual.

MATLAB (R2019a) fits the kinetics using the pseudo-first-order, pseudo- second-order, Elovich, and intra-particle diffusion models. The isothermal mod- els of diverse materials are investigated by Langmuir, Temkin, Freundlich, Dubinin Radushkeivch, and Harkins–Jura.

3 Results and Discussion

3.1 Adsorption STUDIES and EFFECT of Operating Parameters

The removal efficiency of the produced adsorbents tests against 1000 ppm M.O dye. In addition, the removal efficiency is investigated at pH levels ranging from 3 to 9, contact times between the adsorbent and M.O ranging from 15 to 180 min., and M.O concentration ranging from 25 to 1000 ppm. Shaking at 120 rpm and room temperature is used to carry out all adsorption processes.

3.1.1 Screening Test and Effect of pH

In this section, the screening experiment is combined with the effect of pH to get the best adsorbent materials, as shown in Fig. 3. The various produced materials of nZVI, Fe^0-Cu, and different AC-Fe^0-Cu are screened by treating 10 ml of 1000 ppm of the synthetic M.O solution with 0.01 g of the adsorbent. Different pH values of 3, 5, 7, and 9 are used simultaneously to determine the best pH value of which adsorbent. The obtained results indicate that as the pH value is decreased, the removal efficiency of M.O increases. That is due to the positive surface charges and more robust interactions with anionic M.O dye (pH = 3). At pH = 3, the removal efficiency of the adsorbent materials varied from 93.44% to 97.34%

3.1.2 Effect of Contact Time

The bimetallic Fe^0-Cu, H_2SO_4 chemical AC-Fe^0-Cu, and commercial AC-Fe^0-Cu are selected from the screening test, which has the best removal efficiencies among the produced adsorbent materials, with removal capacities of 678.66, 666.65, and 679.47 mg/g, respectively. The impact

Fig. 3 Screening experiment with applied different pH values for Methyl orange removal using different prepared adsorbent materials
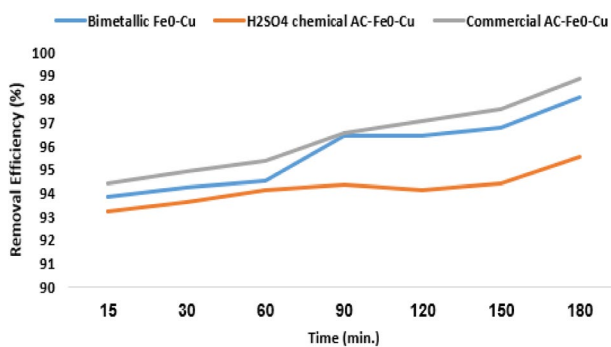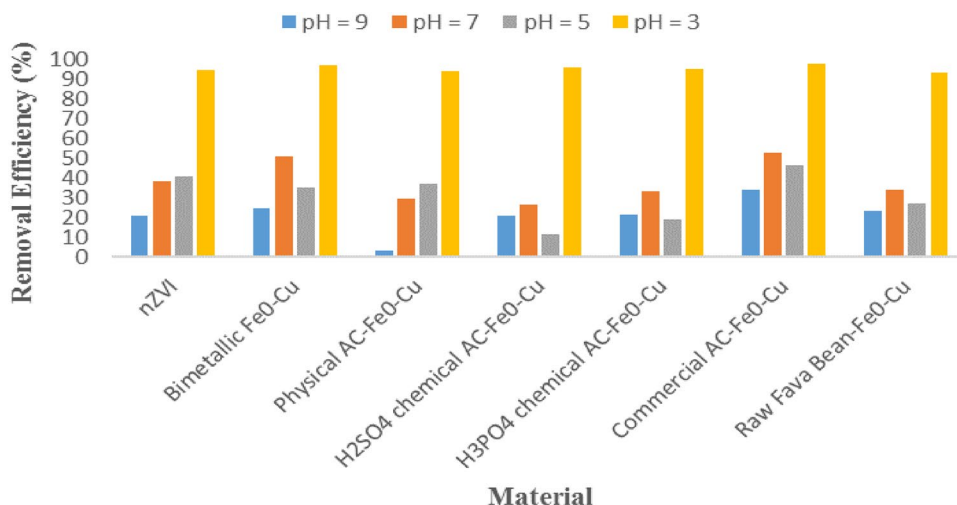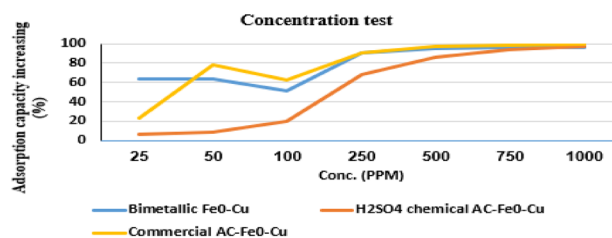

Fig. 4 Contact time experiment for Methyl Orange removal using bimetallic Fe^0-Cu, H_2SO_4 chemical AC-Fe^0-Cu, and commercial AC-Fe^0-Cu

Fig. 5 Effect of different Methyl orange concentrations on the adsorption capacity using bimetallic Fe0-Cu, H2SO4 chemical AC-Fe0-Cu, and commercial AC-Fe0-Cu
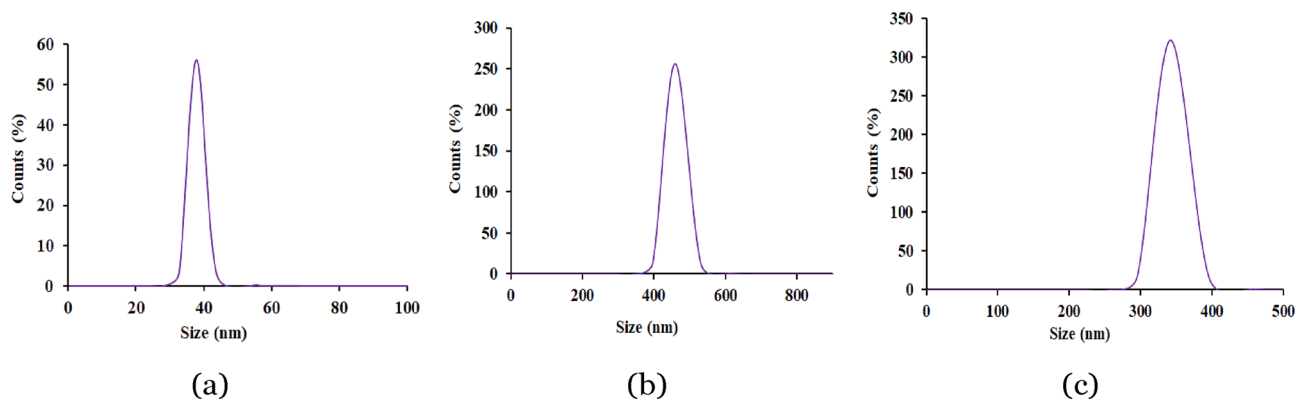
1000 ppm at the optimal time and pH values (3 h and pH 3), as shown in Fig. 5. The Adsorption capacity increases as the initial concentration of dye increases. Raising the initial concentration increases the moving power of the dye molecules from the bulk to the adsorbent material surface.

3.2 Characterization of Adsorbent Materials

DLS, FT-IR, XRD, and SEM are used to Characterize the selected adsor- bents (bimetallic Fe^0-Cu, H_2SO_4 chemical AC-Fe^0-Cu, and commercial AC- Fe^0-Cu) as follows:

3.2.1 Dynamic Light Scattering (DLS) Results

The particle size and charge of the chosen adsorbents are determined using DLS, as illustrated in Fig. 6 and summarized in Table 1. At pH = 3, these charges neutralize and become positive, which may be owing to the protonation of the adsorbents' amino groups to be more suitable to adsorb and remove the anionic M.O dye. All prepared adsorbents are in nanoscale, with dimensions of 37.84, 458.66, and 341.9 nm for Fe^0-Cu, H_2SO_4 chemical AC-Fe^0-Cu, and commercial AC-Fe^0-Cu, respectively.

of contact time is investigated by combining the same dose of 0.01 g of adsorbent material and 10 ml of 1000 ppm dye solution at room temperature with shaking at 120 rpm and various contact times of 15, 30, 60, 90, 120, 150, and 180 min, as shown in Fig. 4. The optimum residence time to reach the highest removal efficiency by Bimetallic F e0-Cu, H2SO4 chemical AC-Fe0-Cu, and commercial AC-Fe0-Cu is 180 min. science, 97.2%, 94.3%, and 99.1% are the achieved removal efficiency by Bimetallic F e0-Cu, H2SO4 chemical AC-Fe0-Cu, and commercial AC-Fe0-Cu, respectively. The contact time tests show that as the contact time increases, the removal efficiency increases. Bimetallic Fe^0-Cu, H_2SO_4 chemical AC-Fe^0-Cu, and commercial AC-Fe^0-Cu have equilibrium removal capacities of 779.62, 759.59, and 786.03 mg/g, respectively.

3.1.3 Effect of Concentration

The chosen adsorbent materials are tested to absorb different concentrations of M.O dye of 25, 50, 100, 250, 500, 750, and

Fig. 6 DLS results of **a** bimetallic Fe^0-Cu, **b** H_2SO_4 chemical AC-Fe^0-Cu, and **c** commercial AC-Fe^0-Cu

Table 1 DLS potential of the prepared adsorbent materials

| Material name	DLS (nm)
Bimetallic Fe0-Cu	37.84
H2SO4 chemical AC-Fe0-Cu	458.66
Commercial AC-Fe0-Cu	341.9

3.2.2 Fourier Transition Infrared (FT-IR) Results

FTIR is considered one of the most important characterization methods used to detect functional groups on the surface of adsorbent materials: Fig. 7 and Table 2 represent the FTIR analysis and the copious functional groups detected on the surface of the three types of adsorbents bimetallic Fe0-Cu, H2SO4 chemical AC-Fe^0-Cu, and commercial AC-Fe^0-Cu. A copious functional group detected for both bimetallic Fe^0-Cu, and commercial AC-F e0 -Cu adsorbent materials state their highest capacity for M. orange removal than H2SO4 chemical AC-Fe^0-Cu as represented in Fig. 6.

The spectra of the bimetallic Fe0 -Cu showed a strong peak at 3383.1 Cm^{-1} associated with OH and NH stretching polyphenols, and the one at 2975.43 Cm^{-1} is assigned to CH-CH2 stretching aliphatic group. The peak that appeared within the range 2100–2550 Cm^{-1} is associated with the C=C conjugated C–C. Another beak that appeared at 1923.41 Cm^{-1} is associated with Carboxyl acid. The peak that appeared at 1650.28 Cm^{-1} is associated with the C=O Amide I band. The peak that appeared within the range (1400–1460) Cm^{-1} is associated with the stretching inorganic carbonate C=O. Another beak that appeared at 1381.87 Cm^{-1} is associated with CH and CH2 aliphatic bending groups. The peak that appeared within the range (1240–1340) Cm^{-1} is associated with the C-N Amide III band. The peak that appeared at 1088.01 Cm^{-1} is associated with the P=O from phospholipids. The peak that appeared at 1048.24 Cm^{-1} is associated with the

Alkyl amine. Another beak that appeared within the range (800–900) Cm^{-1} is associated with C=C, C=N, C–H in the ring structure. The peak that appeared at 655.75 Cm^{-1} is associated with the C=O bending. Another beak that appeared at 434.58 Cm^{-1} is associated with Alkyl halides. The spectra of the H2SO4 chemical AC-F e0 -Cu showed a strong peak at 3442.54 Cm^{-1} is associated with the OH of carbohydrates. The peak that appeared at 2984.81 Cm^{-1} is associated with the CH of the aromatic ring. The peak that appeared at 2090.19 Cm1 is associated with the C=C conjugated and C ≡ C. The peak that appeared at 1635.13 Cm1 is associated with the 1635.13. Another beak that appeared within the range (1400–1460) Cm^{-1} is associated with stretching –C=O inorganic carbonate. The peak that appeared at 1166.88 Cm1 is associated with C–O–C polysaccharide a. The peak that appeared at 1082.34 Cm^{-1} is associated with the P=O from phospholipids. The peak that appeared at 1044.54 Cm^{-1} is associated with the Alkyl amine group. Another beak that appeared at 568.54 Cm^{-1} is associated with the Alkyl halides.

The spectra of commercial AC-Fe^0 -Cu showed a strong peak at 3650.45 Cm1 is associated with the OH stretching vibration. The peak that appeared at 3423.58 Cm^{-1} is associated with the OH of carbohydrates. The peak that appeared at 2962.25 Cm^{-1} is associated with the CH3 stretching asym. The peak that appeared at 2923.5 Cm^{-1} is associated with CH and CH2 aliphatic stretching groups. The peak that appeared at 2853.53 Cm^{-1} is associated with the C-H stretching sym. of > CH2 in fatty acid chains, -CH2 stretching sym. methylene chains in membrane lipids Saturated fatty acids. Another beak that appeared at 1662.59 Cm1 and 1637.73 Cm^{-1} is associated with Amide I of proteins. The peak that appeared at 1379.63 Cm^{-1} is associated with the C=O stretching sym. of COO-: fatty acids and amino acids. The peak that appeared at 1166.79 Cm^{-1} is associated with the ester C–O–C str., asym. -C–O ester str., single bond mainly phospholipids. Another beak that appeared at
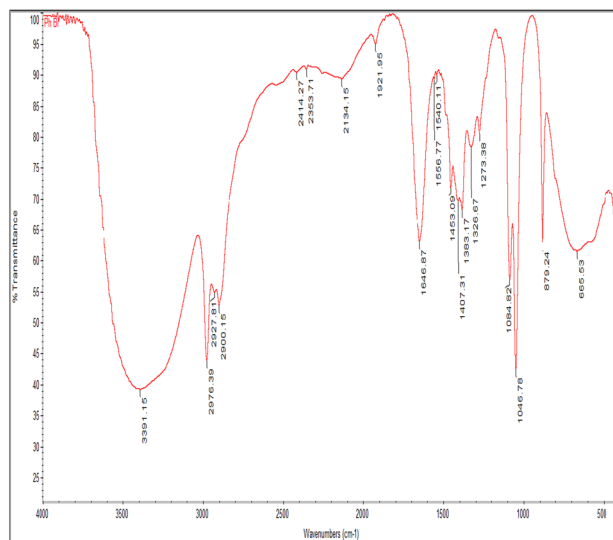
(a)
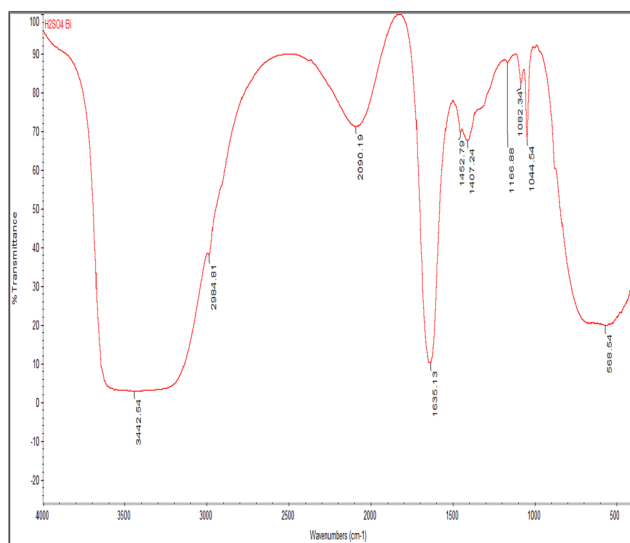
(b)
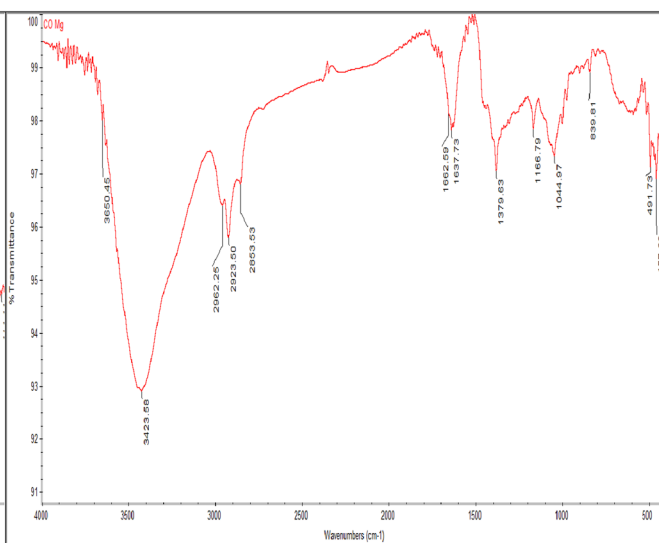
(c)

Fig. 7 FT-IR spectrum of **a** bimetallic Fe^0-Cu, **b** H_2SO_4 chemical AC-Fe^0-Cu, and **c** commercial AC-Fe^0-Cu

1044.97 Cm^{-1} is associated with the Glycogen band due to OH str. coupled with -C-O str.-C-O of C OH groups of carbohydrates. Another beak that appeared at 839.81 Cm^{-1} is associated with an Aromatic plane ring with 2 neighboring C-H groups. A small peak that appeared at 491.73 Cm^{-1} is associated with the Alkyl halide groups.

3.2.3 X‑Ray Diffraction (XRD) Analysis Results

The amorphous shape appears in different images of Fig. 8. The peak at $2\theta = 44.5°$ proves the existence of zero-valent iron Fe^0 [39]. The peak of activated carbon is at $2\theta = 24°$.

However, the nZVI surface peaks at $2\theta = 35°$, which corresponds to the iron oxides Fe_2O_3 and Fe_3O_4. The presence of Fe_2O_3 and Fe_3O_4 is induced by partial oxidation of nZVI during processing and transfer, which produces oxides on the surface of adsorbents [40].

3.2.4 Scanning Electron Microscope (SEM) Results

The surface morphology of the adsorbents is investigated by a scanning elec- tron microscope (SEM), as shown in Fig. 9. The synthesized bimetallic Fe^0-Cu particles (Fig. 8a) have a semi-spherical shape with an average size of 434.03 nm. It looks like a huge nanocluster, which might be owing to

Table 2 FT-IR spectrum of (a) bimetallic Fe^0-Cu, (b) H_2SO_4 chemical AC-Fe^0-Cu, and (c) commercial AC-Fe^0-Cu

FT-IR peak (cm^{-1})	Assigned functional group
(a) Bimetallic Fe^0-Cu	
3383.1	*OH*, NH stretching polyphenols
2975.43	CH-CH2 stretching aliphatic group
2100–2550	C=C conjugated C–C
1923.41	Carboxyl acid
1650.28	C=O Amide I band
1400–1460	stretching inorganic carbonate C=O
1381.87	CH and CH2 aliphatic bending group
1240–1340	C-N Amide III band
1088.01	P=O from phospholibids
1048.24	Alkyl amine
800–900	C=C, C=N, C–H in ring structure
655.75	C=O bending
434.58	Alkyl halides
(b) $H2SO4$ chemical AC-Fe^0-Cu	
3442.54	*OH* of carbohydrates
2984.81	CH of aromatic ring
2090.19	C=C conjugated and $C \equiv C$
1635.13	C=O Amide I band
1400–1460	stretching –C=O inorganic carbonate
1166.88	C–O–C polysaccharide a
1082.34	P=O from phospholibids
1044.54	Alkyl amine
568.54	Alkyl halides
(c) Commercial AC-Fe^0-Cu	
3650.45	*OH* stretching vibration
3423.58	*OH* of carbohydrates
2962.25	CH3 str., asym
2923.5	CH and CH2 aliphatic stretching group
2853.53	C-H str., sym. of > CH2 in fatty acid chains, -CH2 str., sym. methylene chains in membrane lipids Saturated fatty acids
1662.59	Amide I of proteins
1637.73	Amide I of proteins
1379.63	C=O str., sym. of COO-: fatty acids and amino acids
1166.79	ester C–O–C str., asym. -C–O ester str., single bond mainly phospholipids
1044.97	Glycogen band (due to *OH* str. coupled with σ) -C-O str. -C-O σ of $C-OH$ groups of carbohydrates
839.81	Aromatic-out-of plane ring with 2 neighbouring C-H group
491.73	Alkyl halides

magnetic forces between the nanoparticles. Many pores in the bimetallic Fe^0-Cu nanoparticles allow the M.O dye impurities to be transported better. (Fig. 8b) The H_2SO_4 chemical AC has a huge semi-continuous surface with a spraying of Fe^0-Cu nanoparticles with numerous fractures to absorb the M.O dye impurities. (Fig. 8c) shows a commercial AC that has been covered with Fe^0-Cu nanoparticles with an average size of 314.23 nm. There is a broad surface area with numerous holes to facilitate the absorption of MO dye contaminants.

3.3 Kinetics Study

The Pseudo-first-order, Pseudo-second-order, and Intra-particle diffusion mod- els are applied to fit the results of bimetallic Fe^0-Cu, H_2SO_4 chemical AC- Fe^0-Cu, and commercial AC-Fe^0-Cu adsorption using MATLAB(R2019a) as illustrated in Tables 3, 4, and 5. By identifying characteristics and employing kinetic models, the adsorption kinetics study seeks to characterize and quantify the adsorption process. The kinetics of adsorption is

determined using various kinetic models that are tailored to the experimental data. To determine which kinetic model best fits the experimental data, the computed results from the kinetic models are contrasted with the data, and the highest correction factor is detected. For example, for adsorption kinetic, pseudo-first-order kinetic, and intra-particle diffusion models, which are implemented for each type of adsorbent [41]. The experimental data were fit by pseudo-first-order (PFO), pseudo-second-order (PSO), and intra-particle models. As shown in Tables 3, 4, and 5, The pseudo-second-order is the best fit for bimetallic F e0–Cu with R2 = 0.9913. The pseudo-first-order is the best fit for H2SO4 chemical AC-F e0-Cu with R2 = 0.902. The Intra-particle diffusion is the best fit for commercial AC-F e0-Cu with R2 = 0.94. Table 6 shows the evaluation of the kinetic model parameters.

(a) (b) (c)
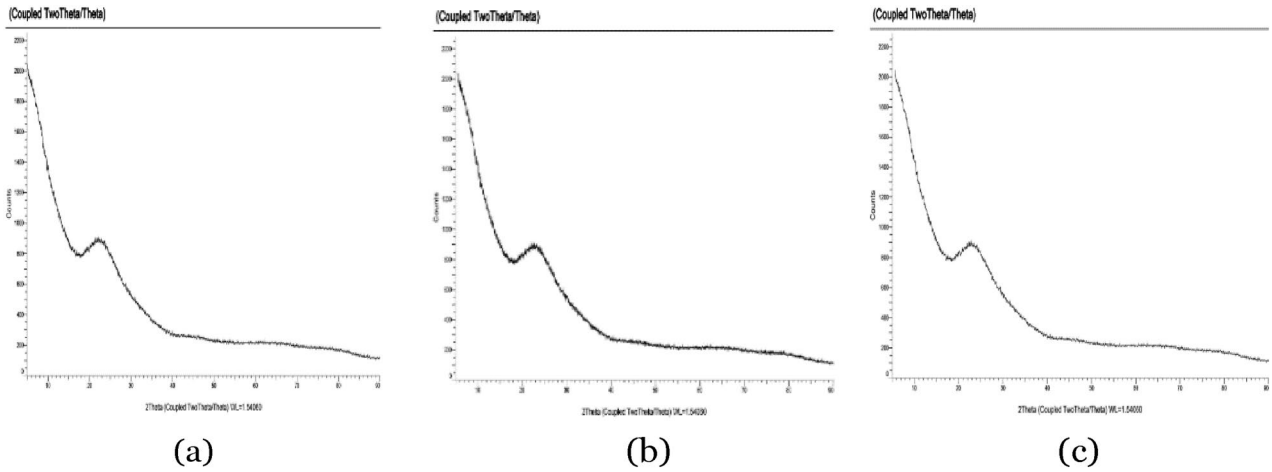
Fig. 8 XRD analysis of **a** bimetallic Fe^0-Cu, **b** H_2SO_4 chemical AC-Fe^0-Cu, and **c** commercial AC-Fe^0-Cu

(a) (b) (c)
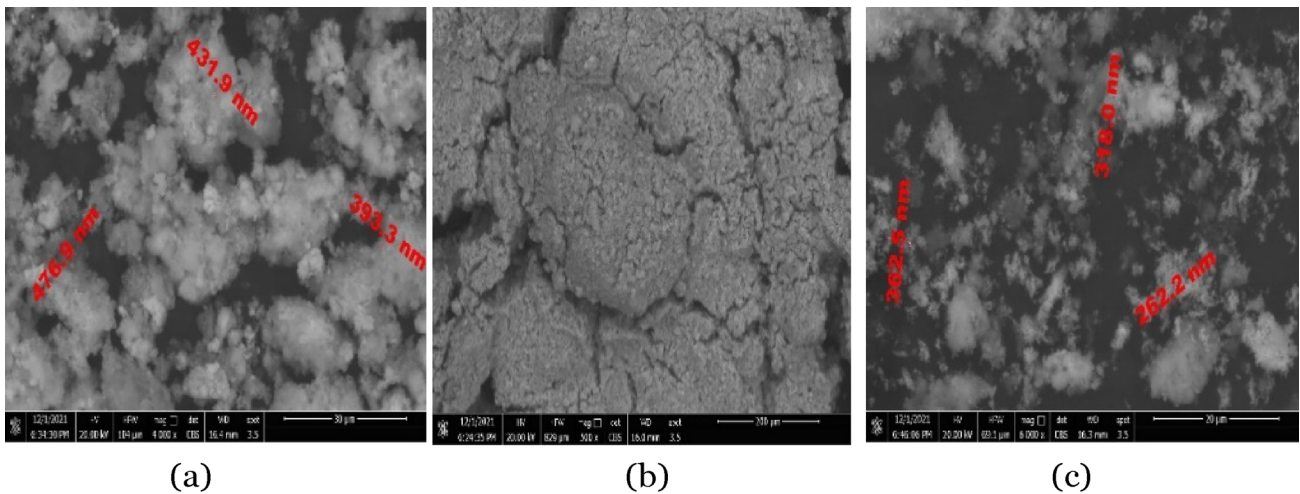
Fig. 9 SEM images of **a** bimetallic Fe^0-Cu, **b** H_2SO_4 chemical AC-Fe^0-Cu, and **c** commercial AC-Fe^0-Cu

Table 3 Comparison between nonlinear kinetic models for M.O removal by bimetallic Fe^0 Cu

Name	Model	Math. model	Curve fitting	R^2
Pseudo first order	Nonlinear	$q_t = q_e(1 - e^{-K_1 t})$	$y = 767.6(1 - e^{-0.1243x})$	0.9852
Pseudo second order	Nonlinear	$q_t = \frac{K_1 t q_e^2}{1 + K_1 t q_e}$	$y = \frac{774.2x}{x + 0.9986}$	0.9913
Intra- particle diffusion	Nonlinear	$q_t = K_{int}\sqrt{t} + C_{int}$	$y = 3.024\sqrt{x} + 734.1$	0.914

3.3.1 The Pseudo-First-Order and The Pseudo-Second-Order Adsorption Kinetic Models

Most of the adsorption kinetic research conducted over the last two decades modeled their kinetic datasets using the traditional PFO and PSO rate laws. These two models have been used to investigate a variety of adsorption systems. As contaminants or adsorbates, biomass, nanomaterials, heavy metals, and medicines are all possible. Ho and McKay (1999) evaluated several literature datasets using the linear versions of these two models. Since then, the models have grown in popularity, PSO more so than PFO because it can fit most kinetic datasets and is thus regarded as the better of the two. Because these models are so widely used, they have generated a modeling practice cul- ture that introduces uncertainty and inaccuracies that are frequently ignored or dismissed. The pseudo-first-order and pseudo-second-order Adsorption kinetic models are introduced mathematically [42].

3.3.2 Intra-Particle Diffusion Model

The absorption mechanism is either particle diffusion control or film diffusion control. Before adsorption, several diffusion mechanisms are known to influence the adsorption process to occur. Before entering the sorbent's micropores and macropores, the sorbate must diffuse through most of the solution to the film surrounding the adsorbent. The first is bulk diffusion resistance, which naturally decreases with enough agitation to reduce the concentration gradient. The resistance to external mass transfer is the second, and intra-particle mass transfer is the third. When the rate-limiting step is the last, intraparticle diffusion controls the sorption mechanism. The Intra particle diffusion model's mathematical form is introduced [43].

3.4 Isotherm Models

Isothermal models include Temkin, Freundlich, Dubinin-Radushkeivch (DR), and Nonlinear Langmuir models. The state of equilibrium of an adsorption isotherm describes the process of a substance being adsorbed on a surface while the temperature remains constant. It shows how much substance is bonded to the surface of the substance in the solution. The adsorbate is the substance that must be removed during the adsorption process, and the adsorbent is the material onto which it is adsorbed. Adsorption isotherms are used to calculate the affinity of the adsorbate for the adsorbent. To provide experimental data, the nonlinear Langmuir, Temkin, Freundlich, and Dubinin-Radushkeivch(DR) models

Table 4 Comparison between nonlinear kinetic models for M.O removal by H_2SO_4 chemical $AC-Fe^0-Cu$

Name	Model	Math. model	Curve fitting	R^2
Pseudo first order	Nonlinear	$q_t = q_e(1 - e^{-K_1 t})$	$y = 748.9(1 - e^{-0.1701x})$	0.902
Pseudo second order	Nonlinear	$q_t = \frac{K_1 t q_e^2}{1+K_1 t q_e}$	$y = \frac{751.2x}{x+0.2646}$	0.847
Intra- particle diffusion	Nonlinear	$q_t = K_{int}\sqrt{t} + C_{int}$	$y = 0.809\sqrt{x} + 741$	0.6354

Table 5 Comparison between nonlinear kinetic models for M.O removal by commercial $AC-Fe^0-Cu$

Name	Model	Math. model	Curve fitting	R^2
Pseudo first order	Nonlinear	$q_t = q_e(1 - e^{-K_1 t})$	$y = 765.9(1 - e^{-0.1405x})$	0.4918
Pseudo second order	Nonlinear	$q_t = \frac{K_1 t q_e^2}{1+K_1 t q_e}$	$y = \frac{774x}{x+0.8379}$	0.7801
Intra- particle diffusion	Nonlinear	$q_t = K_{int}\sqrt{t} + C_{int}$	$y = 3.256\sqrt{x}\, 735.6$	0.94

Table 6 Kinetic parameters for different models for the adsorption process of M.O using bimetallic $Fe^0 - Cu$, H_2SO_4 chemical $AC-Fe^0-Cu$, and commercial $AC-Fe^0-Cu$

Kinetic models	Parameters	Values		
		Bimetallic Fe^0–Cu	H_2SO_4 chemical AC–Fe^0–Cu	Commercial AC –Fe^0–Cu
Pseudo 1st order	q_e(mg/g)	767.6	748.9	765.9
	K_1(1/min)	0.1243	0.1701	0.1405
Pseudo 2nd order	q_e(mg/g)	774.2	751.2	774
	K_1(1/min)	0.0013	0.005	0.0015
Intra-particle diffusion	K_{int}(mg/gmin$^{0.5}$)	3.024	0.809	3.256
	C_{int}(mg/g)	734.1	741	735.6

are chosen [44]. The Dubinin-Radushkeivch (DR) model is the best fit for the bimetallic Fe0Cu, as shown in Table 7. The concentration experiments' results are consistent with the isotherm models. As illustrated in Tables 7, 8, and 9. Langmuir, Freundlich, Temkin, and Dubinin Radushkeivch (DR) mod- els are used to fit the data for M.O removal by bimetallic Fe^0-Cu, H_2SO_4 chemical AC-Fe^0-Cu, and commercial AC-Fe^0-Cu. Freundlich and DR models are the best fit results for bimetallic Fe^0-Cu and H_2SO_4 chemical AC-Fe^0- Cu, with $R^2 = 0.9367$ and $R^2 = 0.9908$ for bimetallic Fe^0-Cu, and with R^2 values of 0.9996 and 0.9995, respectively. Freundlich is the best fit model for M.O removal by commercial AC-Fe^0-Cu, with $R^2 = 0.9674$. The adsorption

is physisorption for the three different adsorbents. The isotherm parameters are evaluated as shown in Table 10. The Freundlich and the DR models have a high R-square; however, the mean free energy (E) is higher than 8, as shown in Table 10. Therefore, adsorption is Physisorption. The maximum amount adsorbed q_e equals 1174 calculated from the DR model for the bimetallic Fe^0 Cu. The maximum amount adsorbed q_e equals 1200 calculated from the Langmuir model for the bimetallic Fe^0 Cu, as shown in 10.

Table 7 Comparison between Isothermal models for M.O removal by bimetallic $Fe^0 - Cu$

Type	Name	Adsorbent surface	Math. model	Curve fitting	R^2
Chemisorption	Langmuir	Homogeneous	$q_e = \frac{q_m K_L C_e}{1 + K_L C_e}$	$y = \frac{1200x}{x + 32.48}$	0.6431
	Temkin	The binding energy is uniformly distributed	$q_e = \frac{RT}{b} \ln(K_T C_e)$	$y = 468.8\ln(0.1602x)$	0.8521
Physisorption	Freundilch	Heterogeneous	$q_e = K_F \times C_e^{\frac{1}{n}}$	$y = 2.204 X^{1.794}$	0.9367
	Dubinin-Radushkeivch	Heterogeneous	$q_e = q_m e^{-Kad\left[RTln\left(1 + \frac{1}{C_e}\right)\right]^2}$	$y = 1174 e^{-299.8\ln^2\left(1 + \frac{1}{x}\right)}$	0.9908

Table 8 Comparison between Isothermal models for M.O removal by H_2SO_4 chemical $AC - Fe^0 - Cu$

Type	Name	Adsorbent surface	Math. model	Curve fitting	R^2
Chemisorption	Langmuir	Homogeneous	$q_e = \frac{q_m K_L C_e}{1 + K_L C_e}$	$y = \frac{1020x}{x + 697.7}$	0.5169
	Temkin	The binding energy is uniformly distributed	$q_e = \frac{RT}{b} \ln(K_T C_e)$	$y = 72.62 \ln(0.05567x)$	0.575
Physisorption	Freundilch	Heterogeneous	$q_e = K_F * C_e^{\frac{1}{n}}$	$y = 9.982 \times 10^{-10} x X^{6.229}$	0.9996
	Dubinin-Radushkeivch	Heterogeneous	$q_e = q_m e^{-Kad\left[RTln\left(1 + \frac{1}{C_e}\right)\right]^2}$	$y = 1014 e^{-7711\ln^2\left(1 + \frac{1}{x}\right)}$	0.9995

Table 9 Comparison between Isothermal models for M.O removal by commercial AC-$Fe^0 - Cu$

Type	Name	Adsorbent surface	Math. model	Curve fitting	R^2
Chemisorption	Langmuir	Homogeneous	$q_e = \frac{q_m K_L C_e}{1 + K_L C_e}$	$y = \frac{600x}{x + 112.2}$	0.6255
	Temkin	The binding energy is uniformly distributed	$q_e = \frac{RT}{b} \ln(K_T C_e)$	$y = 72.59\ln(0.1868x)$	0.5654
Physisorption	Freundlich	Heterogeneous	$q_e = K_F * C_e^{\frac{1}{n}}$	$y = 0.0005037 x X^{3.788}$ $e^{-7711\ln^2\left(1 + \frac{1}{x}\right)}$	0.9674
	Dubinin-Radushkeivch	Heterogeneous	$q_e = q_m e^{-Kad\left[RTln\left(1 + \frac{1}{C_e}\right)\right]^2}$	$y = 1014 e^{-7711\ln^2\left(1 + \frac{1}{x}\right)}$	0.9663

Table 10 Isothermal adsorption parameters for different models for the adsorption process of M.O using bimetallic $Fe^0 - Cu$, H_2SO_4 chemical AC $- Fe^0 - Cu$, and commercial AC- Fe^0- Cu

Isotherm models	Parameters	Values		
		Bimetallic $Fe^0–Cu$	$H2SO4$ chemical $AC –Fe^0–Cu$	Commercial $AC –Fe^0–Cu$
Langmuir	$q_{(max)}$	1200	1020	600
	K_L(L/mg)	0.030788	0.00143	0.0089
Freundlich	n	0.55741	0.16054	0.264
	K_F(L/g)	2.204	9.982×10^{-10}	0.0005037
Dubinin-Radushkevich	q_s(mg/g)	1174	1014	576.9
	K_{ad}(mol²/KJ^2)	0.000048	0.00124	0.00017
	E(kJ/mol)	102.1	20.08	54.233
Temkin	β_T	468.8	72.62	72.59
	K_T(L/g)	0.1602	0.05567	0.1868

3.4.1 Temkin Model

Temkin's isotherm model considers the effect of indirect adsorbate/adsorbate interactions on the adsorption process and assumes that increasing surface coverage results in a linear decrease in the heat of adsorption for all molecules in the layer. The Temkin isotherm is only applicable at intermediate ion concentrations. The Temkin model's mathematical form is introduced [45].

3.4.2 Freundlich Model

The Freundlich isotherm governs adsorption activities on heterogeneous sur- faces. This isotherm provides an equation that characterizes the exponential distribution of energy and surface heterogeneity at active sites. The linear form of the Freundlich isotherm, as well as the adsorption capacity and intensity, show how the energy is distributed relatively and how heterogeneous the adsorbate sites are [45].

3.4.3 Dubinin-Radushkeivch (DR) Model

The Dubinin-Radushkeivch isotherm model, an empirical adsorption model, is frequently used to represent adsorption mechanisms with Gaussian energy distribution onto heterogeneous surfaces. This isotherm is only suitable for middle ranges of adsorbate concentrations due to its unrealistic asymptotic behavior and failure to anticipate Henry's laws at low pressure. In a semiempirical equa tion, adsorption is modeled as a pore-filling process. It is a fundamental equation that characterizes the adsorption of gases and vapors on microporous sorbents qualitatively. It has a multilayer

structure that involves Van Der Waal's forces, which are important in physical adsorption processes. Langmuir adsorption, which was developed to characterize gas–solid phase adsorption, is used to measure and compare the adsorption capacity of various adsorbents. By balancing, the Langmuir isotherm explains surface coverage [45].

Table 11 The FCCD design matrix for the adsorption using bimetallic Fe^0-Cu

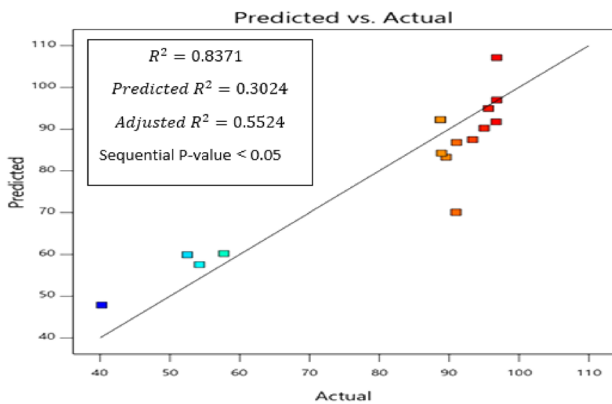| Run	Space type	Concentration	Dose	Time	Removal efficiency
1	Axial	1000	0.75	97.5	96.8
2	Axial	512.5	0.75	15	88.9
3	Axial	512.5	0.5	97.5	89.56
4	Factorial	25	1	15	57.74
5	Center	512.5	0.75	97.5	88.74
6	Factorial	25	0.5	180	54.24
7	Center	512.5	0.75	97.5	88.74
8	Axial	512.5	0.75	180	93.36
9	Factorial	1000	1	180	96.72
10	Axial	25	0.75	97.5	90.98
11	Factorial	1000	0.5	15	95.01
12	Center	512.5	0.75	97.5	88.74
13	Center	512.5	0.75	97.5	88.74
14	Factorial	1000	0.5	180	96.8
15	Factorial	1000	1	15	95.63
16	Center	512.5	0.75	97.5	88.74
17	Factorial	25	1	180	52.49
18	Center	512.5	0.75	97.5	88.74
19	Factorial	25	0.5	15	40.24
20	Axial	512.5	1	97.5	91.05

3.5 Response Surface Methodology (RSM) Optimization for M.O Removal by Bimetallic Fe^0-Cu, H_2SO_4 Chemical AC-Fe^0-Cu, and Commercial AC-Fe^0- Cu

3.5.1 RSM for the Adsorption Using the Bimetallic Fe^0-Cu

The data in Table 11 fits the quadratic model, and the model is generated as follows:

Table 12 The fit summery for the adsorption using bimetallic Fe^0-Cu

Source	Sequential p-value	Adjusted R^2	Predicted R^2	
Linear	0.0011	0.5524	0.3024	Suggested
2FI	0.9099	0.4707	− 1.5308	
Quadratic	0.0394	0.6904	− 0.2205	Suggested
Cubic	0.0699	0.8551	− 55.2238	Aliased

Fig. 10 The predicted removal efficiency versus the actual for the adsorption using bimetallic Fe^0-Cu

$$y = -28.45 + 0.0673x_1 + 200.852x_2$$
$$+ 0.30356x_3 - 0.0156x_1x_2 - 0.000018x_1x_3$$
$$- 0.12091x_2x_3 - 0.000015x_1^2$$
$$- 115.97x_2^2 - 0.000944x_3^2 \tag{6}$$

where*by*, x_1, x_2, x_3 are the removal efficiency, concentration, dose, and time, re- spectively. The quadratic and linear models are suggested due to the results of the fit statistics, as shown in Table 12. The quadratic model is not aliased as in the cubic model, and it has $R^2 = 0.8371$, as shown in Fig. 10.

The ANOVA analysis is used to identify the essential factors that affect the removal efficiency, as shown in Table 13. Model terms with P-values less than 0.0500 are significant. In this situation, A is an effective model term, and A is the concentration. The model terms are not important if the value is bigger than 0.1000. Model reduction may enhance the model if there are numerous inconsequential model terms.

3.5.2 RSM for the Adsorption using H_2SO_4 Chemical AC-Fe^0-Cu

The data in Table 14 fits the quadratic model, and the model is generated as follows:

$$y = 3.478 + 0.2498x_1 + 3.8515x_2$$
$$- 0.0225x_3 - 0.00988x_1x_2 - 0.000067x_1x_3$$
$$+ 0.08882x_2x_3 - 0.000151x_1^2$$
$$- 1.8982X_2^2 - 0.00008X_3^2, \tag{7}$$

where*by*, x_1, x_2, x_3 are the removal efficiency, concentration, dose, and time, re- spectively. The quadratic model is recommended based on the fit statistics, as illustrated in Table 15.

Table 13 ANOVA analysis for the adsorption using bimetallic Fe^0-Cu

Source	Sum of Squares	df	Mean Square	F-value	p-value	
Model	4688.86	9	520.98	5.71	0.0059	significant
A-concentration	3432.50	1	3432.50	37.61	0.0001	
B-Dose	31.61	1	31.61	0.3464	0.5692	
C-Time	25.89	1	25.89	0.2837	0.6059	
AB	28.92	1	28.92	0.3168	0.5859	
AC	4.31	1	4.31	0.0472	0.8324	
BC	49.75	1	49.75	0.5451	0.4773	
A^2	36.90	1	36.90	0.4043	0.5391	
B^2	144.47	1	144.47	1.58	0.2369	
C^2	113.46	1	113.46	1.24	0.2909	
Residual	912.69	10	91.27			
Lack of Fit	912.69	5	182.54			
Pure Error	0.0000	5	0.0000			
Cor Total	5601.55	19				

Table 14 The FCCD Centered design matrix for the adsorption using H_2SO_4 chemical AC-Fe^0-Cu

Run	Space type	Concentration	Dose	Time	Removal efficiency
1	Factorial	1000	0.5	180	95.47
2	Factorial	25	1	15	10.5
3	Center	512.5	0.75	97.5	91.71
4	Center	512.5	0.75	97.5	91.71
5	Axial	1000	0.75	97.5	95.71
6	Center	512.5	0.75	97.5	91.71
7	Axial	512.5	0.75	15	92.04
8	Factorial	1000	1	180	96.18
9	Factorial	25	1	180	27.99
10	Axial	512.5	0.5	97.5	91.38
11	Center	512.5	0.75	97.5	91.71
12	Factorial	25	0.5	15	12.25
13	Factorial	1000	0.5	15	96.1
14	Center	512.5	0.75	97.5	91.71
15	Center	512.5	0.75	97.5	91.71
16	Axial	512.5	0.75	180	92.04
17	Axial	25	0.75	97.5	15.75
18	Factorial	1000	1	15	96.25
19	Axial	512.5	1	97.5	91.38
20	Factorial	25	0.5	180	15.75

Table 15 The fit summery for the adsorption using H_2SO_4 chemical AC-Fe^0-Cu

Source	Sequential p-value	Adjusted R^2	Predicted R^2	
Linear	0.0001	0.6569	0.5084	
2FI	0.9769	0.5841	− 0.7061	
Quadratic	< 0.0001	0.9969	0.9716	Suggested
Cubic	< 0.0001	1.0000	0.9919	Aliased
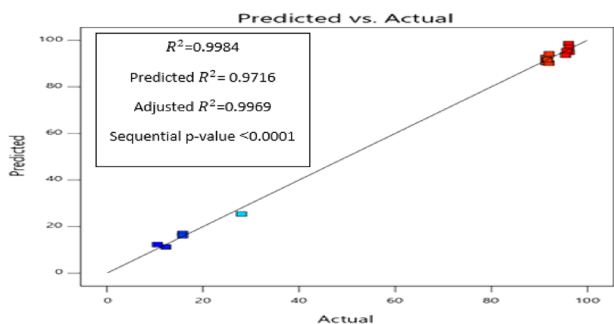
Fig. 11 The predicted removal efficiency versus the actual for the adsorption using H2SO4 chemical AC-Fe0-Cu

The quadratic model is not aliased as in the cubic model, and it has $R^2 = 0.9984$, as shown in Fig. 11.

The ANOVA analysis is used to identify the essential factors that affect the removal efficiency, as shown in Table 16. Model terms with P-values less than 0.0500 are significant. A, C, AC, BC, and A^2 are crucial model terms in this scenario, where A denotes concentration, B denotes dosage, and C denotes time. The model terms are not important if the value is bigger than 0.1000. Model reduction may enhance the model if there are numerous inconsequential model terms.

3.5.3 RSM for the Adsorption Using the Commercial AC-Fe⁰-Cu

The data in Table 17 fits the quadratic model, and the model is generated as follows:

$$
\begin{aligned}
y = {} & -1.656 + 0.2243x_1 + 15.274x_2 \\
& + 0.1282x_3 + 0.0021x_1x_2 - 0.00005x_1x_3 \\
& + 0.0133x_2x_3 - 0.000138x_1^2 \\
& - 10.6036x_2^2 - 0.000413x_3^2
\end{aligned}
\tag{8}
$$

where*by, x_1, x_2, x_3 are the removal efficiencies with different concentration, dose, and time, respectively. The quadratic model is recommended based on the fit statistics, as illustrated in Table 18. The quadratic model is not aliased as in the cubic model, and it has $R^2 = 0.999$, as shown in Fig. 12.

The ANOVA analysis is used to identify the essential factors that affect the removal efficiency, as shown in Table 19. Model terms are significant if their P-values are less than 0.0500. A, C, AC, A^2, and C^2 are important model variables in this situation, where A represents concentration and C represents time. The model terms are not significant if their values exceed 0.1000. Model reduction may enhance the model if there are a lot of inconsequential model terms.

3.6 Artificial Neural Network (ANN)

Deep learning techniques depend on neural networks, also known as artificial neural networks (ANNs) or simulated neural networks (SNNs), which are a subset of neural networks. AI stands for machine learning. Their structure and nomenclature are modeled after the human brain, mirroring organic neuron communication. Each node, or artificial neuron, is linked to others and has its own weight and threshold. Any node whose output exceeds a predefined threshold value is activated and sends data to the network's top layer. If not, information from the next network level is retained. An artificial neural network (ANN) node layer consists of an input layer, one or more hidden layers, and an output layer.

Table 16 ANOVA analysis for the adsorption for H_2SO_4 chemical AC-Fe^0-Cu

| Source	Sum of Squares	df	Mean Square	F-value	p-value	
Model	22,256.56	9	2472.95	680.48	< 0.0001	significant
A-concentration	15,798.24	1	15,798.24	4347.17	< 0.0001	
B-Dose	12.88	1	12.88	3.54	0.0891	
C-Time	41.17	1	41.17	11.33	0.0072	
AB	11.59	1	11.59	3.19	0.1044	
AC	58.81	1	58.81	16.18	0.0024	
BC	26.46	1	26.46	7.28	0.0224	
A^2	3518.34	1	3518.34	968.13	< 0.0001	
B^2	0.0387	1	0.0387	0.0107	0.9198	
C^2	0.8060	1	0.8060	0.2218	0.6478	
Residual	36.34	10	3.63			
Lack of Fit	36.34	5	7.27			
Pure Error	0.0000	5	0.0000			
Cor Total	22,292.90	19				

Table 17 The FCCD Centered design matrix for the adsorption using commercial AC-Fe^0-Cu

Run	Space type	Concentration	Dose	Time	Removal efficiency
1	Factorial	25	0.5	180	20
2	Axial	512.5	0.75	15	85.93
3	Center	512.5	0.75	97.5	90.06
4	Center	512.5	0.75	97.5	90.06
5	Factorial	1000	1	180	94.93
6	Axial	512.5	1	97.5	92.04
7	Factorial	1000	0.5	15	92.67
8	Axial	512.5	0.5	97.5	88.24
9	Factorial	25	1	15	10
10	Center	512.5	0.75	97.5	90.06
11	Axial	25	0.75	97.5	21
12	Factorial	1000	0.5	180	92.83
13	Axial	1000	0.75	97.5	94.93
14	Factorial	25	0.5	15	10
15	Axial	512.5	0.75	180	90.06
16	Factorial	25	1	180	19.25
17	Center	512.5	0.75	97.5	90.06
18	Factorial	1000	1	15	91.82
19	Center	512.5	0.75	97.5	90.06
20	Center	512.5	0.75	97.5	90.06

Table 18 The fit summery for the adsorption using commercial AC-Fe^0-Cu

Source	Sequential p-value	Adjusted R^2	Predicted R^2	
Linear	0.0001	0.6543	0.4966	
2FI	0.9949	0.5768	− 0.8673	
Quadratic	< 0.0001	0.9985	0.9927	Suggested
Cubic	0.0043	0.9997	0.8946	Aliased
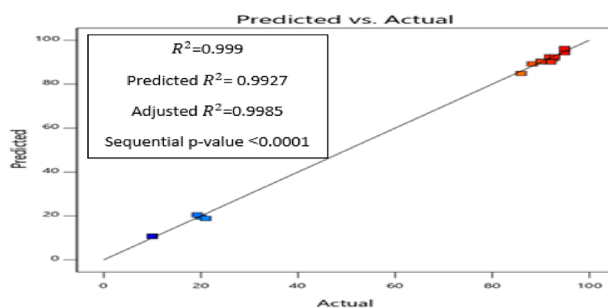
Fig. 12 The predicted removal efficiency versus the actual for the adsorption using com- mercial AC-Fe^0-Cu

Three neurons make up the input layer: concentration, dose, and time. The removal efficiency is represented by one neuron in the output layer. The hidden layer's neuron count ranged from 3 to 15, and in most adsorption techniques, ten is the best number that achieves a minor error. The input data is normalized to be in the 0 to 1 range. The network's input variables were dosage, contact time, and temperature, while the network's output variable was removal efficiency.

the layer from which the network output. It was claimed that the experimental data set obtained by using the RSM was enough to properly assess the ANN model. ANN is applied to the same data of RSM that is shown in Tables 11, 14, and 17. ANN is implemented using MATLAB (R2019a), and the feed-forward network is selected. The network is made up of three layers: an input layer, a hidden layer, and an output layer, where the input and output layer contain three neurons and one neuron, respectively. The number of neurons in the hidden layer is ten after experimenting with other values.

Table 19 ANOVA analysis for the adsorption using commercial AC-Fe^0-Cu

Source	Sum of Squares	df	Mean Square	F-value	p-value	
	21,205.51	9	2356.17	1362.03	< 0.0001	significant
A-concentration	14,971.48	1	14,971.48	8654.59	< 0.0001	
B-Dose	1.85	1	1.85	1.07	0.3256	
C-Time	71.02	1	71.02	41.06	< 0.0001	
AB	0.5000	1	0.5000	0.2890	0.6026	
AC	31.92	1	31.92	18.45	0.0016	
BC	0.6050	1	0.6050	0.3497	0.5674	
A^2	2965.37	1	2965.37	1714.20	< 0.0001	
B^2	1.21	1	1.21	0.6982	0.4229	
C^2	21.68	1	21.68	12.53	0.0054	
Residual	17.30	10	1.73			
Lack of Fit	17.30	5	3.46			
Pure Error	0.0000	5	0.0000			
Cor Total	21,222.81	19				

That has the smallest mean square error. Tansig is the transfer function between the input and hidden layers, while a pure line (Purline) is the transfer function between the hidden and output layers. The ANN has a higher R^2 values than the RSM models, as confirmed in the regression plots shown in supplementary figures (S-1,S-2,S-3).

The data set was split into three groups; 70% of them were used to train the network, 15% to validate it, and the remaining 15% to test the results. The test set independently assessed the performance of the network. The validation set modified the network's bias, variance, and generalization. R2019b MATLAB was utilized as the programming language, and TensorFlow was used for the ANN calculations. The training, validation, testing, and overall correction factors are obtained in supplementary figures (S-1,S-2,S-3).for bimetallic F e0 -Cu, H2SO4 chemical AC-F e0 -Cu, and commercial AC-F e0–Cu, respectively.

Table 11 indicates experimental removal efficiency, RSM predicted removal efficiency, RSM residual, ANN predicted removal efficiency, and ANN residual for the bimetallic F e0–Cu. Tables 14 and 17 obtain experimental removal efficiency, RSM predicted removal efficiency, RSM residual, ANN pre dicted removal efficiency, and ANN residual for H2SO4 chemical AC-F e0 -Cu, and commercial AC-F e0–Cu, respectively. The previous values in all these Tables 11, 14, and 17 are obtained through 20 runs with three different space types (factorial, axial, and center). Five neurons are the best number in the case of using Bimetallic F e0–Cu. In Table 11 for the Bimetallic F e0 -Cu, the best experimental and predicted removal efficiency is 96.8% RE (through runs 1, and 14). In Table 14 for H2SO4 chemical AC-F e0 -Cu, the best experimental and predicted removal efficiency is 96.25% RE (through run 18). In Table 17 for the commercial AC-F e0–Cu, the best experimental and predicted removal efficiency is 94.93%RE (through run 5).

The use of artificial neural networks (ANN) for mapping, regression, modeling, clustering, classification, and multivariate data analysis is gaining popularity. The ANN is a multivariate statistical technique used to describe a wide range of mathematical objects and processes. Nonlinearity, which allows for a better fit to the data; noise insensitivity, which provides accurate prediction in the presence of uncertain data and measurement errors; high parallelism, which implies fast processing and hardware failure tolerance; learning and adaptability, which allows the system to update (modify) its internal structure in response to changing environment and generalization are the main advantages of ANN. artificial neural networks (ANNs) have been routinely used to predict dye adsorption. This research applies the uses of ANN approaches for dye adsorption, including multilayer feedforward neural networks (MLFNN). These ANNs models are gaining prominence as techniques that can be used successfully for dye adsorption with acceptable accuracy.

3.7 Optimization Results

The maximum removal efficiency is achieved at optimum conditions, which are evaluated by optimizing RSM quadratic model and the ANN model. First, numerical optimization is applied to the RSM model using Design-Expert software. Then, the Moth Search Algorithm (MSA) is applied to the ANN model to get the optimum conditions that maximize the removal efficiency. A metaheuris- tic algorithm is used to optimize ANN. Metaheuristic combines one main word (heuristic) and suffix (meta) that have roots in Greek. The term (heuristic) is an old Greek word that means discovering new rules in dealing with different problems, and the term (meta) means some upper-level methodologies in na- ture. The metaheuristics use higher-level approaches to

implement a searching process that can avoid the optimum local result and find the global optimum [46]. Many applications use these algorithms, such as extracting optimized bio-impedance model parameters using different typologies of oscillators and Plant stem tissue modelling and parameter identification using metaheuristic opti-mization algorithms [47, 48]. Moth Search Algorithm (MSA) is selected to be combined with ANN (ANN + MSA). The nocturnal behavior of moths inspires MSA [49]. The results of these optimization methods are shown in supplementary table (S-1), which are validated experimentally as shown in the confirmation column. The maximum removal efficiency is 98.66% by using Bimetallic Fe^0-Cu according to the confirmation of ANN + MSA results. The error of ANN + MSA is 1.8%, and the RSM model error is 4.2% in the case of using Bimetallic Fe^0-Cu. RSM and ANN + MSA give almost the same result when using the chemical AC-Fe-Cu. However, RSM gives better results than ANN + MSA when using commercial AC-Fe-Cu.

4 Conclusion

The anionic M.O dye was used to screen the prepared adsorbents of nZVI, bimetallic Fe^0-Cu, physical AC-Fe^0-Cu, H_2SO_4 chemical AC-Fe^0-Cu, H_3PO_4 chemical AC-Fe^0-Cu, commercial AC-Fe^0-Cu, and raw fava bean-Fe^0-Cu. The most significant removal efficiencies were obtained by bimetallic Fe^0-Cu, H_2SO_4 chemical AC-Fe^0-Cu, and commercial AC-Fe^0-Cu. The most efficient adsorbent materials were characterized using DLS, FT-IR, XRD, and SEM.

Bimetallic Fe^0-Cu has a removal capacity of 995.96 mg/g at (pH = 3, 180 min. contact time under shaking at 120 rpm at room temperature, 1000 ppm of M.O, and 1 g/l dose of bimetallic Fe^0-Cu adsorbent). The pseudo-second-order is the best fit for bimetallic Fe^0-Cu with $R^2 = 0.9913$. H_2SO_4 chemical AC-Fe^0-Cu adsorbent has a removal capacity of 990.35 mg/g at (pH = 3, 180 min. contact time under shaking at 120 rpm at ambient temperature, 1000 ppm of M.O, and 1 g/l dose of H_2SO_4 chemical AC-Fe^0-Cu adsorbent).

The pseudo-first-order is the best fit for H_2SO_4 chemical AC-Fe^0-Cu with $R^2 = 0.902$. At (pH = 3, 180 min. contact time under shaking at 120 rpm at room temperature, 1000 ppm M.O, and 1 g/l dose of commercial AC-Fe^0-Cu adsorbent), the removal capacity of commercial AC-Fe^0-Cu adsorbent is 977.53 mg/g. Intra-particle diffusion is the best fit for commercial AC-Fe^0-Cu with $R^2 = 0.94$. The isothermal results show that physisorption is involved in adsorption and that multi-layers develop on the adsorbent surface.

The experimental data were fit by pseudo-first-order (PFO), pseudo-second-order (PSO), and intra-particle models. The pseudo-second-order is the best fit for bimetallic F e0 -Cu with $R^2 = 0.9913$. The pseudo-first-order is the best fit for H2SO4 chemical AC-Fe^0-Cu with $R^2 = 0.902$. The Intra-particle diffusion is the best fit for commercial AC- Fe^0-Cu with $R^2 = 0.94$. The Dubinin-Radushkeivch (DR) model is the best fit for the bimetallic Fe0Cu. The Freundlich and the DR models have a high R-square; however, the mean free energy (E) is higher than 8 Therefore, adsorption is Physisorption.

The maximum amount adsorbed q_e equals 1174 was calculated from the DR model for the bimetallic Fe0Cu. The maximum amount of adsorbed material q_e equals 1200 calculated from the Langmuir model for the bimetallic Fe0Cu. The Bimetallic Fe^0-Cu, the best experimental and predicted removal efficiency is 96.8% RE (through runs 1, and 14). For the H2SO4 chemical AC-Fe^0-Cu, the best experimental and removal efficiency is 96.25% RE (through run 18). The commercial AC-Fe^0–Cu, the best experimental and predicted removal efficiency is 94.93%RE (through run 5). That is clear low-cost adsorbents such as Bimetallic Fe0-Cu, and Fava Bean Activated Carbon-Supported Bimetallic AC-Fe0-Cu can remove the Methyl orange dye with a high removal efficiency which is competed for the commercial and chemical adsorbents.

Declarations

References

1. Peng H, Guo J (2020) Removal of chromium from wastewater by membrane filtration, chemical precipitation, ion exchange, adsorption electro coagulation, electrochemical reduction, electrodialysis, electrode ionization, photocatalysis and nanotechnology: a review. Environ Chem Lett 18:2055–2068

2. Chakraborty R, Asthana A, Singh AK, Jain B, Susan ABH (2022) Adsorption of heavy metal ions by various low-cost adsorbents: a review. Int J Environ Anal Chem 102:342–379

3. Eltaweil AS, El-Tawil AM, Abd El-Monaem EM, El-Subruiti GM (2021) Zero valent iron nanoparticle-loaded nanobentonite intercalated carboxymethyl chitosan for efficient removal of both anionic and cationic dyes. ACS Omega 6:6348–6360

4. Guan X, Sun Y, Qin H, Li J, Lo IM, He D, Dong H (2015) The limitations of applying zero-valent iron technology in contaminants seques- tration and the corresponding countermeasures: the development in zero- valent iron technology in the last two decades (1994–2014). Water Res 75:224–248

5. Rashid T, Iqbal D, Hazafa A, Hussain S, Sher F, Sher F (2020) Formulation of zeolite supported nano-metallic catalyst and applications in textile effluent treatment. J Environ Chem Eng 8:104023

6. Badawi AK, Zaher K (2021) Hybrid treatment system for real textile wastewater remediation based on coagulation/flocculation, adsorption and filtration processes: Performance and economic evaluation. J Water Process Eng. 40:101963

7. Ahmad M, Akanji MA, Usman AR, Al-Farraj AS, Tsang YF, Al-Wabel MI (2020) Turning date palm waste into carbon nanodots and nano zerovalent iron composites for excellent removal of methylthioninium chloride from water. Sci Rep 10:16125

8. Satapanajaru T, Yoo-iam M, Bongprom P, Pengthamkeerati P (2015) Decolorization of reactive black 5 by persulfate oxidation activated by ferrous ion and its optimization. Desalin Water Treat 56:121–135

9. Velusamy S, Roy A, Sundaram S, Kumar Mallick T (2021) A review on heavy metal ions and containing dyes removal through graphene oxide based adsorption strategies for textile wastewater treatment. Chem Rec 21:1570–1610

10. Scaria J, Nidheesh P, Kumar MS (2020) Synthesis and applications of var- ious bimetallic nanomaterials in water and wastewater treatment. J Environ Manage 259:110011

11. Li Y, Zhao H-P, Zhu L (2021) Remediation of soil contaminated with organic compounds by nanoscale zero-valent iron: A review. Sci Total Environ 76:143413

12. Sharma G, Kumar A, Sharma S, Naushad M, Dwivedi RP, Alothman ZA, Mola GT (2019) Novel development of nanoparticles to bimetallic nanoparticles and their composites: a review. J King Saud Unive -Sci. 31:257–269

13. Etim U, Umoren S, Eduok U (2016) Coconut coir dust as a low cost adsorbent for the removal of cationic dye from aqueous solution. J Saudi Chem Soc 20:S67–S76

14. Chen Q, Tang Z, Li H, Wu M, Zhao Q, Pan B (2020) An electron-scale comparative study on the adsorption of six divalent heavy metal cations on mnfe2o4@ cac hybrid: experimental and dft investigations. Chem Eng J 381:122656

15. Tan X-F, Zhu S-S, Wang R-P, Chen Y-D, Show P-L, Zhang F-F, Ho S-H (2021) Role of biochar surface characteristics in the adsorption of aromatic compounds: Pore structure and functional groups. Chin Chem Lett 32(10):2939–2946

16. Chen Y (2011) Synthesis, characterization and dye adsorption of ilmenite nanoparticles. J Non-Cryst Solids 357(1):136–139

17. Anderson A, Anbarasu A, Pasupuleti RR, Manigandan S, Praveenkumar T, Kumar JA (2022) Treatment of heavy metals containing wastewater using biodegradable adsorbents: A review of mechanism and future trends. Chemosphere 295:133724

18. Han H, Rafiq MK, Zhou T, Xu R, Mašek O, Li X (2019) A critical review of clay-based composites with enhanced adsorption performance for metal and organic pollutants. J Hazard Mater 369:780–796

19. Bayomie OS, Kandeel H, Shoeib T, Yang H, Youssef N, El-Sayed MM (2020) Novel approach for effective removal of methylene blue dye from water using fava bean peel waste. Sci Rep 10(1):1–10

20. Semba RD, Ramsing R, Rahman N, Kraemer K, Bloem MW (2021) Legumes as a sustainable source of protein in human diets. Glob Food Sec 28:100520

21. Zohry AE-H, Ouda SA (2017) "Solution for faba bean production- consumption gap", in future of food gaps in Egypt. Springer. https://doi.org/10.1007/978-3-319-46942-3_6

22. Makled S, Fawzy ST et al (2019) Egyptian demand for faba beans from the most important international import markets. Arab Univer J Agricult Sci 27(2):1325–1337

23. Nahali L, Miyah Y, Mejba F, Benjelloun M, Assila O, Fahoul Y, Nenov V, Zerrouq F (2022) Assessment of brilliant green and eriochrome black t dyes adsorption onto fava bean peels: kinetics, isotherms and re-generation study. Desal Water Treat 245:255–269

24. Nahali L, Miyah Y, Mejba F, Benjelloun M, Assila O, Fahoul Y, Nenov V, Zerrouq F (2022) Assessment of brilliant green and eriochrome black t dyes adsorption onto fava bean peels: kinetics, isotherms and regen- eration study. Desal Water Treat 245:255–269

25. Mitra S, Mukherjee T, Kaparaju P (2021) Prediction of methyl orange removal by iron decorated activated carbon using an artificial neural net- work. Environ Technol 42(21):3288–3303

26. Karri RR, Tanzifi M, Tavakkoli Yaraki M, Sahu J (2018) Optimization and modeling of methyl orange adsorption onto polyaniline nano-adsorbent through response surface methodology and differential evolution embedded neural network. J Environm Manag. 223:517–529

27. Tanzifi M, Hosseini SH, Kiadehi AD, Olazar M, Karimipour K, Rezaiemehr R, Ali I (2017) Artificial neural network optimization for methyl orange adsorption onto polyaniline nano-adsorbent: Kinetic, isotherm and thermodynamic studies. J Mol Liq 244:189–200

28. Saini K, Sahoo A, Biswas B, Kumar A, Bhaskar T (2021) Preparation and characterization of lignin-derived hard templated carbon (s): Statistical optimization and methyl orange adsorption isotherm studies. Biores Technol 342:125924

29. Hamdy A, Mostafa MK, Nasr M (2018) Zero-valent iron nanoparticles for methylene blue removal from aqueous solutions and textile wastewater treatment, with cost estimation. Water Sci Technol 78(2):367–378

30. Eljamal O, Thompson IP, Maamoun I, Shubair T, Eljamal K, Lueangwattanapong K, Sugihara Y (2020) Investigating the design param- eters for a permeable reactive barrier consisting of nanoscale zero-valent iron and bimetallic iron/copper for phosphate removal. J Mol Liq 299:112144

31. Bouchelta C, Medjram MS, Bertrand O, Bellat J-P (2008) Preparation and characterization of activated carbon from date stones by physical ac- tivation with steam. J Anal Appl Pyrol 82(1):70–77

32. Pallarés J, González-Cencerrado A, Arauzo I (2018) Production and char- acterization of activated carbon from barley straw by physical activation with carbon dioxide and steam. Biomass Bioenerg 115:64–73

33. Liu Q-S, Zheng T, Wang P, Guo L (2010) Preparation and characteri- zation of activated carbon from bamboo by

microwave-induced phosphoric acid activation. Ind Crops Prod 31(2):233–238

34. Hubbe MA, Hasan SH, Ducoste JJ (2011) Cellulosic substrates for removal of pollutants from aqueous systems: A review. metals. BioRe- sources 6(2):2161–2287

35. Yahya MA, Al-Qodah Z, Ngah CZ (2015) Agricultural bio-waste mate- rials as potential sustainable precursors used for activated carbon produc- tion: A review. Renew Sustain Energy Rev 46:218–235

36. Samsuri A, Sadegh-Zadeh F, Seh-Bardan B (2014) Characterization of biochars produced from oil palm and rice husks and their adsorption ca- pacities for heavy metals. Int J Environ Sci Technol 11(4):967–976

37. Chang C, Lian F, Zhu L (2011) Simultaneous adsorption and degrada- tion of γ-hch by nzvi/cu bimetallic nanoparticles with activated carbon support. Environ Pollut 159(10):2507–2514

38. Abdel-Aziz HM, Farag RS, Abdel-Gawad SA (2019) Carbamazepine removal from aqueous solution by green synthesis zero-valent iron/cu nanoparticles with ficus benjamina leaves' extract. Int J Environm Res 13(5):843–852

39. Ansari A, Siddiqui VU, Akram MK, Siddiqi WA, Khan A, Al-Romaizan AN, Hussein MA, Puttegowda M (2021) Synthesis of atmospher- ically stable zero-valent iron nanoparticles (nzvi) for the efficient catalytic treatment of high-strength domestic wastewater. Catalysts 12(1):26

40. Mandal S, Pu S, Wang X, Ma H, Bai Y (2020) Hierarchical porous struc- tured polysulfide supported nzvi/biochar and efficient immobilization of se- lenium in the soil. Sci Total Environ 708:134831

41. Husien S, El-taweel RM, Mohamed N, Abdel-Aziz A, Alrefaey K, Elshabrawey SO, Mostafa NG, Said LA, Fahim IS, Radwan AG (2023) Potentials of algae-based activated carbon for the treatment of m orange in wastewater. Chem Environm Eng. 10:0330

42. Revellame ED, Fortela DL, Sharp W, Hernandez R, Zappi ME (2020) Adsorption kinetic modeling using pseudo-first order and pseudo-second order rate laws: A review. Clean Eng Technol 1:100032

43. Yoro KO, Amosa MK, Sekoai PT, Mulopo J, Daramola MO (2020) Diffusion mechanism and effect of mass transfer limitation during the adsorption of co2 by polyaspartamide in a packed-bed unit. Int J Sustain Eng 13(1):54–67

44. Abin-Bazaine A, Trujillo AC, Olmos-Marquez M (2022) "Adsorption isotherms: Enlightenment of the phenomenon of adsorption. Wastewa- ter Treat. https://doi.org/10.5772/intechopen.104260

45. Ayawei N, Ebelegi AN, Wankasi D (2017) Modelling and interpretation of adsorption isotherms. J chem 2017:1

46. Talatahari S, Azizi M (2021) Chaos game optimization: a novel metaheuristic algorithm. Artif Intell Rev 54(2):917–1004

47. Ghoneim MS, Mohammaden AA, Mohsen M, Said LA, Radwan AG (2021) A modified differentiator circuit for extracting cole-impedance model parameters using meta-heuristic optimization algorithms. Arab J Sci Eng 46(10):9945–9951

48. Ghoneim MS, Gadallah SI, Said LA, Eltawil AM, Radwan AG, Madian AH (2022) Plant stem tissue modeling and parameter identification using metaheuristic optimization algorithms. Sci Rep 12(1):1–17

49. Mohamed A-AA, Mohamed YS, El-Gaafary AA, Hemeida AM (2017) "Optimal power flow using moth swarm algorithm. Elect Power Syst Res. 142:190–206